The Canadian Mineralogist
Vol. 42, pp. 371-392 (2004)

EMPLACEMENT OF VISCOUS MUSHES IN THE JINCHUAN ULTRAMAFIC INTRUSION, WESTERN CHINA

SYBRAND A. DE WAAL[§] and ZHANGHUA XU

Centre for Research on Magmatic Ore Deposits, Department of Geology, University of Pretoria, Pretoria 0002, South Africa

CHUSI LI

Department of Geological Sciences, Indiana University, Bloomington, Indiana 47405, U.S.A.

HASSINA MOURI

Centre for Research on Magmatic Ore Deposits, Department of Geology, University of Pretoria, Pretoria 0002, South Africa

ABSTRACT

The Jinchuan ultramafic intrusion in western China has an elongate surface expression of about 6000 by 350 meters. It is one of several mafic–ultramafic intrusions found in the fault-bounded Longshoushan uplifted terrane, of Proterozoic age, located along the southwestern edge of the Sino-Korea platform. Three boreholes from the western, central and eastern parts of the intrusion were sampled and studied. The rocks from the Jinchuan intrusion are olivine – orthopyroxene – chromian spinel cumulates with orthopyroxene, clinopyroxene, plagioclase and phlogopite as interstitial phases. On average, base-metal sulfides (pyrrhotite, pentlandite and chalcopyrite) constitute 5 wt% of the rocks. The samples are overprinted by low-grade metamorphism, hydrothermal alteration and near-surface oxidation. Minor chromian spinel and orthopyroxene preceded olivine in the crystallization sequence. Olivine composition varies between Fo_{79} and Fo_{85}. This variation is negatively correlated with the amounts of trapped silicate liquid in the rocks and is ascribed to the effects of subliquidus and metamorphic re-equilibration. The complex and highly variable lithological structures, limited variation in Fo in the olivine and grain sizes suggest that the intrusion was formed by injection of high-yield-strength viscous crystal-mushes containing variable amounts of sulfide liquid and silicate melt of basaltic composition into planar fractures or faults. During mush emplacement at Jinchuan, flow differentiation controlled the proximal, central part of the intrusion, resulting in subconcentric lithological zonation in this regime, whereas chaotic flow prevailed in the distal, eastern and western parts of the intrusion, resulting in complex lithological banding and interfingering. The original emplacement and flow structures did not collapse because of the high viscosity and high yield-strength of the crystal mushes, strong enough to withhold the gravitational forces imposed on the mushes after flow eased. The observed sequence of crystallization in the rocks suggests that the crystal mushes were formed in a staging chamber at a depth between 4 and 9 km. In this staging chamber, olivine-poor magma occurred at the top and olivine-rich mushes containing minor orthopyroxene and chromian spinel, and variable amounts of silicate and sulfide liquids, were concentrated toward the base in response to gravitational settling. The stratified liquid–crystal materials were then squeezed out of the staging chamber into planar fracture or fault systems at higher levels to form a series of mafic–ultramafic intrusions, possibly induced by the collapse of the chamber roof. The roof collapse was probably triggered by regional extension. Early extraction of the crystal-poor magma from the top of the staging chamber formed the sulfide-poor mafic intrusions in the vicinity of the Jinchuan intrusion. Subsequent extraction of the sulfide-bearing crystal mushes from the bottom of the staging chamber formed the Jinchuan intrusion. The overall high sulfide–silicate ratio in the Jinchuan intrusion resulted from preconcentration of sulfide by liquid stratification in the staging chamber.

Keywords: mafic–ultramafic intrusion, magmatic sulfide, magma stratification, crystal mush, flow differentiation, magma emplacement, Jinchuan, China.

SOMMAIRE

L'intrusion ultramafique de Jinchuan, dans la partie occidentale de la Chine, a une expression allongée en surface, environ 6000 par 350 mètres. C'est un parmi plusieurs massifs intrusifs de composition mafique à ultramafique dans le socle faillé en émergence de Longshoushan, d'âge protérozoïque, situé en bordure sud-ouest de la plateforme sino-koréenne. Trois trous de forage, représentatifs des parties ouest, centrale et est de l'intrusion, ont été échantillonnés. Les roches sont des cumulats à olivine – orthopyroxène – spinelle chromifère, avec orthopyroxène, clinopyroxène, plagioclase et phlogopite dans les interstices. En

§ *E-mail address*: sadw@scientia.up.ac.za

moyenne, les sulfures des métaux de base (pyrrhotite, pentlandite et chalcopyrite) constituent 5% (poids) des roches. Les roches ont subi les effets d'un métamorphisme de faible intensité, une altération hydrothermale et une oxydation près de la surface. Une fraction mineure du spinelle chromifère et de l'orthopyroxène ont précédé l'olivine dans la séquence de cristallisation. L'olivine varie entre Fo_{79} et Fo_{85}. Cette variation montre une corrélation négative avec la quantité de liquide silicaté piégé dans ces roches, et serait due plutôt aux effets subliquidus et métamorphiques. Les structures lithologiques, complexes et fortement variables, la variation limitée de la teneur de l'olivine en Fo, et la taille des grains, font penser que l'intrusion s'est mise en place par injection d'une émulsion visqueuse de cristaux + liquide à limite élevée d'élasticité, contenant des proportions variables de liquides sulfuré et silicaté (composition basaltique) dans une fissure ou une faille. Au cours de la mise en place de cette émulsion à Jinchuan, une différenciation par épanchement a régi la partie centrale, proximale, de l'intrusion, ce qui a mené à une zonation subconcentrique des unités lithologiques dans ce régime, tandis qu'un épanchement plus chaotique était important dans les parties plus distales, à l'est et à l'ouest, avec comme résultat un rubanement lithologique et une interdigitation. La mise en place originale et les structures d'épanchement ne se sont pas effondrées, à cause de la viscosité et le seuil d'élasticité élevés de ces émulsions, suffisamment fortes pour contrecarrer les forces dues à la gravitation imposées à mesure que cessait l'épanchement. D'après la séquence de cristallisation observée dans ces roches, les émulsions de cristaux se sont formées dans une chambre transitoire à une profondeur entre 4 et 9 km. Dans cette chambre, le magma à faible teneur en olivine s'est accumulé vers le sommet, et les émulsions à olivine, contenant orthopyroxène et spinelle chromifère accessoires, et des quantités variables de liquides silicaté et sulfuré, se sont accumulées vers la base à cause de la gravité. Les matériaux contenant liquides + cristaux stratifiés ont par la suite subi une extrusion hors de cette chambre par compression, et une injection dans une fracture ou une faille à un niveau supérieur, pour former une série d'intrusions mafiques et ultramafiques, possiblement dues à l'effondrement du toit. Un tel effondrement a probablement été déclenché par une extension régionale. L'extraction précoce du magma à faible teneur en cristaux de la partie supérieure de la chambre est responsable des roches à faible teneur en sulfures près de l'intrusion de Jinchuan. L'extraction subséquente de fractions enrichies en sulfures près de la base de cette chambre a formé l'intrusion de Jinchuan. Le rapport relativement élevé de sulfures à silicates est le résultat d'une préconcentration de la fraction sulfurée par stratification de la fraction liquide dans la chambre transitoire.

(Traduit par la Rédaction)

Mots-clés: intrusion mafique–ultramafique, sulfures magmatiques, stratification des magmas, émulsion de cristaux, différenciation par épanchement, mise en place du magma, Jinchuan, Chine.

Introduction

The Jinchuan ultramafic intrusion, Gansu Province, China, is currently a dyke-like body, dominated by olivine-rich ultramafic rocks containing disseminated sulfides. It was discovered in 1958, and follow-up exploration proved that the intrusion hosted as much as half a billion tonnes of net-textured, disseminated and subordinate massive Ni–Cu–PGE sulfide ores. Mining has been in operation since 1973. An outstanding feature of the intrusion is the high bulk sulfide-to-silicate ratio, and, as a result, the intrusion holds important clues for the genesis and exploration of similar world-class magmatic sulfide deposits.

In this paper, we use new chemical and physical data to evaluate the existing hypotheses on the genesis of the Jinchuan intrusion. These hypotheses range from injection of stratified ultramafic magmas from a staging chamber (Tang 1998a, b, Tang & Li 1995) to root zones of a large layered mafic intrusion (Chai & Naldrett 1992a). We report evidence for the crystallization of cumulus minerals at variable depths. We use these data in conjunction with lithological data to establish a modified genetic model for the Jinchuan intrusion.

Geological Setting

The Jinchuan ultramafic intrusion is situated on the southwestern margin of the Sino-Korean platform (Fig. 1), a triangular continental mass consolidated at the end of the Early Proterozoic, at ~1.9–1.8 Ga (Li & Cong 1980, Yang *et al.* 1986). The Early Proterozoic rocks in the southwestern part of the platform constitute the Longshoushan Group (Pan 1986), which in the Jinchuan region is represented by a fault-bounded, northwest-striking, uplifted terrane with an east–west structural lineation. Shallow basins, filled with Mesozoic and Cenozoic continental sedimentary rocks, flank both sides of the Longshoushan uplifted terrane. To the south is the Qilianshan (Caledonian) fold belt, which embodies a huge thickness of Cambrian–Silurian clastic, carbonate and volcanic rocks. A blueschist and ophiolite belt occurs on the southern flank of the fold belt, and it has been suggested that ancient oceanic crust to the south was subducted northward beneath the Sino-Korean platform (Zhang *et al*. 1984, Yang *et al*. 1986). In this scheme, the Longshoushan uplifted terrane may represent a part of the ancient continent.

The main rock types in the Longshoushan terrane are the highly metamorphosed Early Proterozoic, or possibly Archean, Longshoushan Group (Tang & Li 1995) and a less intensely metamorphosed series of Middle and Upper Proterozoic rocks. The Longshoushan Group comprises the Baijiazuizi and Tamazigou formations in the eastern part of the Longshoushan uplifted terrane. The older Baijiazuizi Formation, believed to be at least partly Archean in age (Jia 1986), is intruded by a granite yielding a U–Pb isotopic (zircon) age of 2.0186

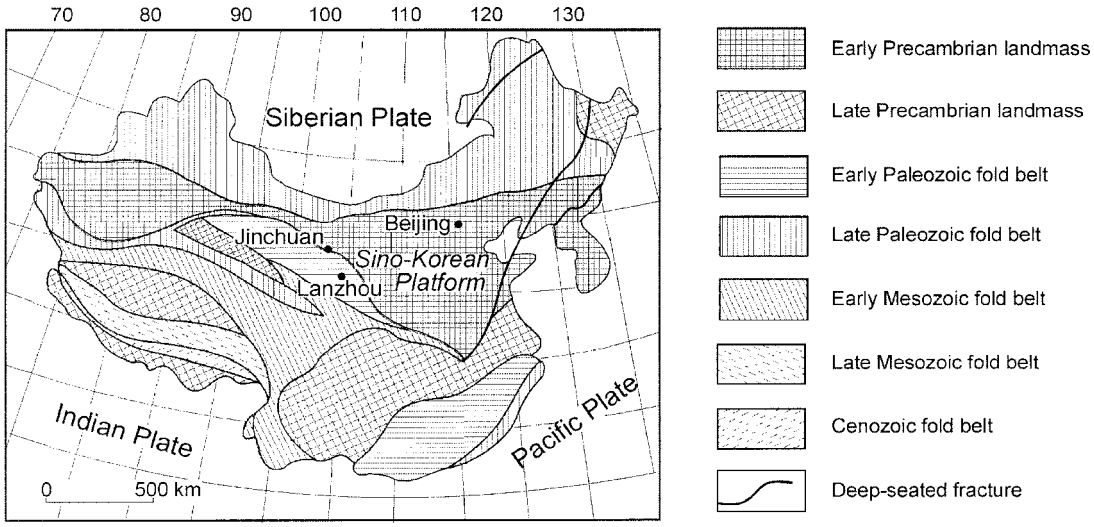

FIG. 1. Regional context of the Jinchuan Ultramafic Intrusion (adapted after Yang *et al*. 1986)

Ga (Tang & Li 1995). The Baijiazuizi Formation consists mainly of migmatite, gneiss and marble (total thickness of more than 3.5 km) and has a faulted contact (denoted F_1, Fig. 2) to the north, which is also the northern boundary of the uplifted terrane. Along this fault, the Baijiazuizi Formation has been pushed up by more than 4 km, and is now directly in contact with post-Paleozoic strata to the north (S. G. U. 1984).

GEOLOGY OF THE INTRUSION

Although the Jinchuan Ni–Cu sulfide deposit was discovered nearly half a century ago, documentation of the deposit (mostly in Chinese) and its host lithology only appeared in publications since the 1980s (Barnes & Tang, 1998, 1999, Chai & Naldrett 1992a, b, 1994, Chai *et al*. 1993, Jia 1986, Li & Cong 1980, Shi 1980, Tang 1982, 1990, 1992, 1998a, b, Tang & Li 1991, 1995, Tang & Ren 1987, Tang *et al*. 1989, 1992; S.G.U. 1984). Chai & Naldrett (1992a, b, 1994) gave detailed summaries of the geology of the Jinchuan Intrusion, and only a brief description is necessary here.

The Jinchuan ultramafic intrusion, which hosts more than 500 million metric tonnes (Mt) of disseminated, net-textured and massive sulfide ore grading 1.06% Ni and 0.7% Cu, outcrops as an elongate body, 6500 m long, usually less than 500 m wide and more than 1100 m deep in its central part (Fig. 2). It intruded marble, migmatite and gneiss of the Baijiazuizi Formation and has a Sm–Nd isochron age of 1.508 ± 0.031 Ga (Tang *et al*. 1992). The central part of the intrusion is relatively well exposed. Its eastern and western ends are covered by Quaternary alluvium.

The intrusion is subdivided into four sections by a series of northeast-trending strike-slip faults (Fig. 2). These four sections, in the order of their discovery, gave rise to the mining areas I, II, III and IV. (S.G.U. 1984). Essential information is summarized in Table 1.

ANALYTICAL METHODS

A total of 125 samples were collected from three boreholes (Figs. 3, 4). Borehole II14–83 represents the central portion of Mining Area II, where the orebodies extend to levels deeper than currently intersected by drilling. Borehole I14–16 lies to the west of II14–83 and represents one of the shallower sections of the orebody. Borehole II48–136 was drilled through a deeper intersection of the orebody to the east of II14–83.

Polished thin sections made from the samples were investigated under a petrographic microscope, and X-ray diffraction of selected samples aided in the identification of the mineral phases present.

All samples were analyzed for major and trace elements on an ARL 8420 wavelength-dispersion XRF spectrometer in the XRF/XRD Laboratory of the Department of Geology, University of Pretoria. Samples were dried and roasted at 950°C to determine percentage loss on ignition (LOI). Major-element analyses were performed on fused beads, following a standard method adapted from Bennett & Oliver (1992). One gram of pre-roasted sample is mixed with 6 g lithium tetraborate flux in a 5% Au/Pt crucible, and fused at 1050°C in a muffle furnace with occasional swirling. Glass disks are poured into a pre-heated Pt/Au mould, with the bottom surface presented for analysis. The samples were analyzed for

TABLE 1. THE FOUR MINING AREAS OF THE JINCHUAN ULTRAMAFIC INTRUSION

	III (West)	I	II	IV (East)
Length	600 m	1500 m	~3000 m	1300 m
Outcrop width	0 to 250 m in east	300 m in west, to 20 m in east	Maximum 530 m	400 m
Shape and dip	Wedge-shaped, SW-dipping	Narrow wedge-shaped, SW-	Tongue-like, steep SW-plunging, lens-shaped in extreme east	Wedge-shaped, SW-dipping
Closure depth	200 m in west to 600 m in east	500 m in west, increasing to 800 m in central part, decreasing to 200 m in east	Closure depth not known; deepest intersection at 1100 m	700 m in the west, becoming shallower eastward
Bounded by	West of F_8	Faults F_8 and F_{16-1}	Faults F_{16-1} and F_{23}	East of F_{23}
Cover	Quaternary alluvium 40 m thick	Well exposed	Well exposed, except for last 300 m toward east	Quaternary alluvium 60 to 140 m thick
Mineralization	Disseminated to net-textured ore	Disseminated to net-textured ore; discovery site	Largest body of massive to net-textured ore in the Jinchuan Intrusion	Disseminated ore

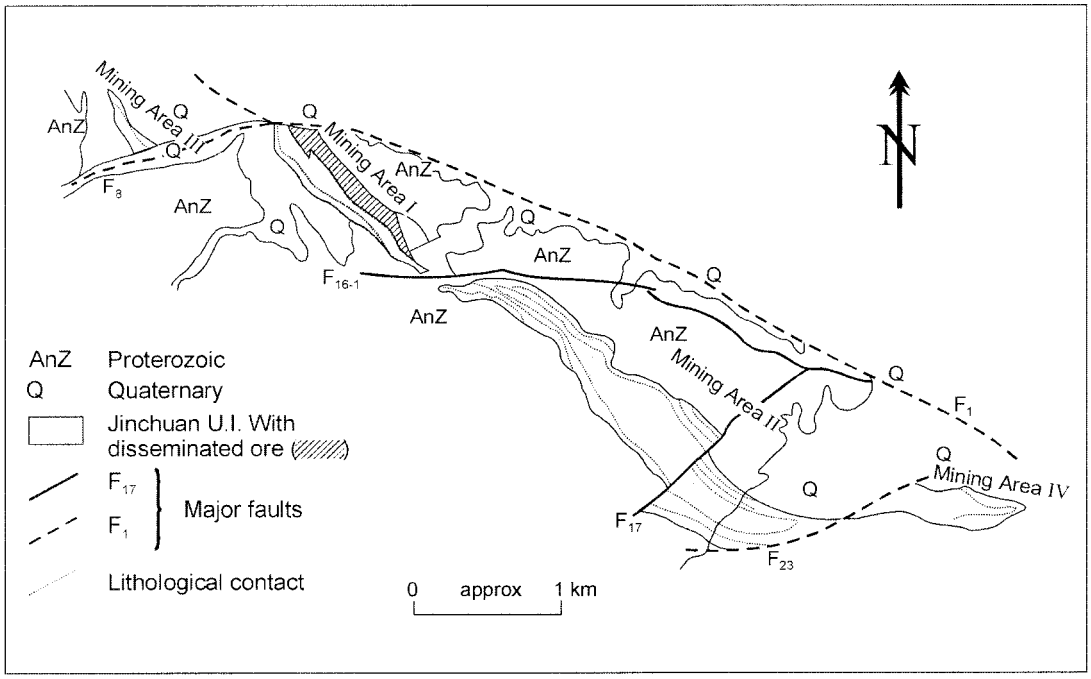

FIG. 2. Geological map of Jinchuan Ultramafic Intrusion (adapted after Jia 1986).

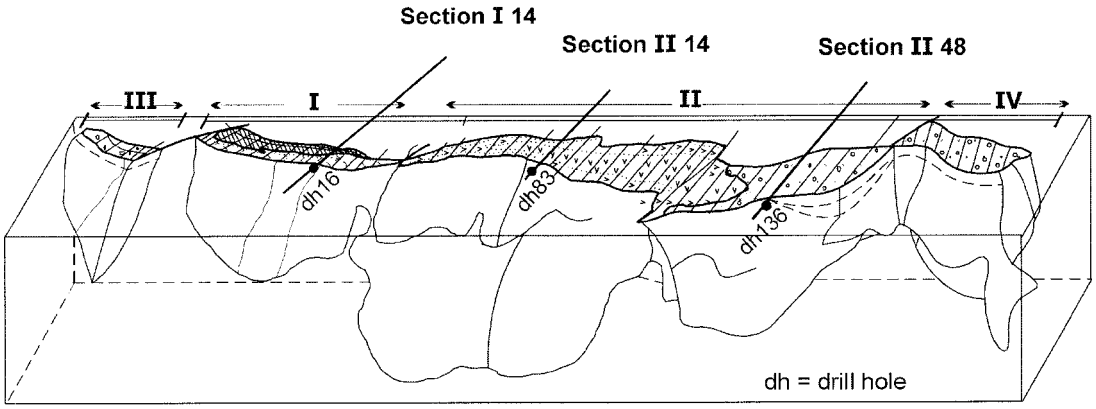

FIG. 3. Oblique three-dimensional view of the Jinchuan Ultramafic Intrusion. Mining areas I, II, III and IV and the position of the boreholes (black dots) on the sections are shown (adapted after Tang & Li 1995). Total length of intrusion ~6.5 km.

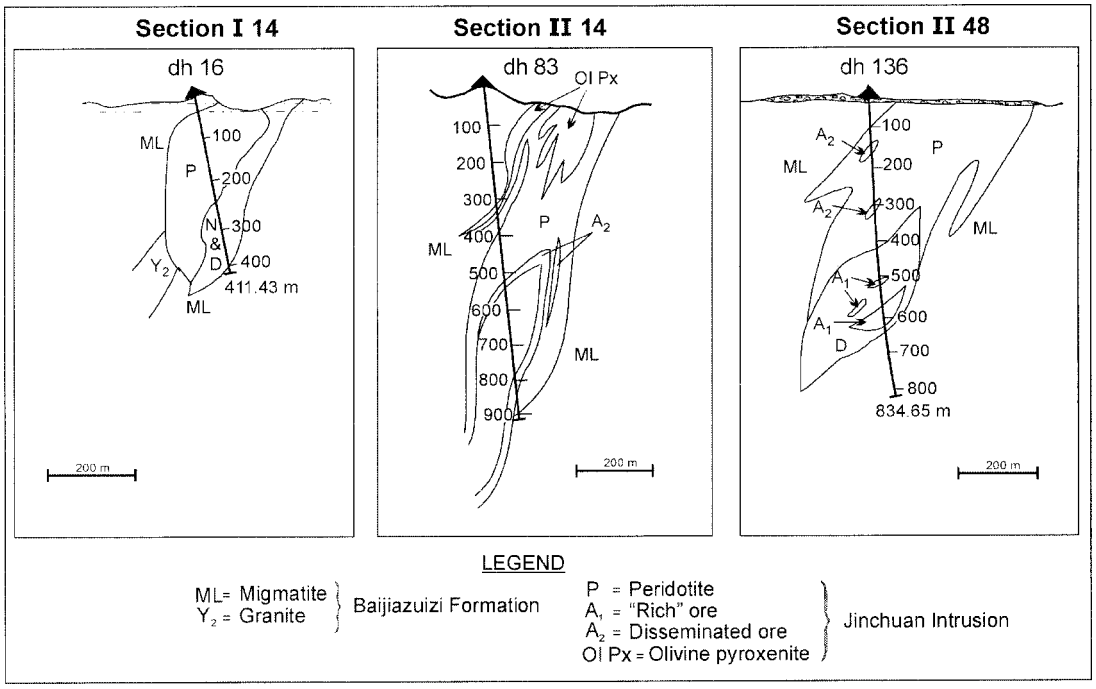

FIG. 4. Profiles showing borehole intersections that were sampled and used in this study. Note the "tongue" (in two dimensions) of sulfide-rich rock (600+ meter high) in borehole II14 –83 and the lensoid lithological boundaries in the other boreholes (adapted after Tang & Li 1995)

selected trace elements on pressed powder pellets with saturated Moviol solution as binder, using an adaptation of the method described by Watson (1996). The XRF spectrometer was calibrated with certified reference materials. The NBSGSC fundamental parameter program was used for matrix correction for the major elements as well as for Cl, Co, Cr, V, Ba and Sc. The Rh Compton peak ratio method was used for the other trace elements. S and CO_2 were determined with an Eltra CS500 carbon–sulfur analyzer.

The chemical composition of the minerals was determined with Cameca SX50 electron microprobes at the University of Indiana (olivine) and at the Université de Paris VI (CAMPARIS) (olivine and other minerals). At Indiana University, we used an accelerating voltage of 15 kV, a beam current of 20 nA and 20 seconds counting intervals for the major elements in the olivine. Nickel in olivine was determined with a 100 nA beam current and 100 seconds counting time. Synthetic oxide and silicate standards were used for calibrations. The accuracies of olivine analyses were determined by analysis of San Carlos olivine (USNM 1113122/444). At the Université de Paris VI, an accelerating voltage of 15 kV, beam current of 20 nA and counting times of 10 to 20 seconds were used. Natural minerals and synthetic oxides served as standards for all elements.

Grain sizes (length and width) of the ten largest grains of olivine observed per thin section were measured under a binocular microscope using a calibrated micrometer scale. This choice of procedure stems from the altered nature of the rocks and the inherent topological constraints. From these measurements, we calculated the square root of the product of the length and width for each grain and averaged over the ten grains per sample. The resulting parameter was used as a relative measure of the grain size in each sample.

All primary chemical and physical data as well as all secondary data calculated from the primary data are available from the Depository of Unpublished Data, CISTI, National Research Council, Ottawa, Ontario K1A 0S2, Canada.

Results

Petrography

Microscopic observations indicate that the rock samples from this study are olivine – orthopyroxene – chromian spinel cumulates. The interstitial materials are either a silicate assemblage of orthopyroxene, clinopyroxene, plagioclase and phlogopite, or a sulfide assemblage of pyrrhotite, pentlandite and chalcopyrite, or variable mixtures of both assemblages.

Olivine is the most abundant primary magmatic silicate in the rocks. It occurs as euhedral to roundish, elongate to equant crystals (maximum aspect-ratio ~2:1). Smaller crystals may occur as inclusions in the pyroxenes. The contents of olivine in the rocks vary from ~40 to >80 wt%. The samples that contain higher quantities of olivine commonly also contain more sulfides.

There are two types of orthopyroxene in the rocks. One occurs as inclusions in olivine (Fig. 5), and the other occurs interstitially with clinopyroxene and plagioclase. The inclusion-type orthopyroxene is small, commonly <1.5 mm in length, with an aspect ratio ~5:1. It constitutes up to 5% by volume in the rocks, but varying from sample to sample. The inclusion-type orthopyroxene is distinguished from the larger and anhedral interstitial grains of orthopyroxene by its euhedral prism-like morphology and low Al and Ca contents (Table 2).

Chromian spinel constitutes <3% by volume in the rocks. The grains are small, mostly <0.03 mm in diameter, and commonly occur as inclusions in both olivine and orthopyroxene. Some contain ilmenite as lamellae or as a reaction rim. The compositions of the chromian spinel are highly variable (Barnes & Tang 1998, 1999).

The samples in this study have been subjected to at least two episodes of metamorphism. In the first stage, interstitial orthopyroxene, clinopyroxene and plagioclase were altered to fine-grained amphibole (tschermakite, actinolite–tremolite), garnet (andradite), chlorite and talc. In the second, lower-temperature stage, olivine was extensively replaced by serpentine ± magnetite, whereas the chromian spinel was commonly altered to an aluminous spinel. At this stage, some orthopyroxene prisms enclosed in olivine also were altered to serpentine, characterized by a bastitic texture.

Signs of shear deformation are observed in some samples, particularly those from the contacts with country rocks and, to a lesser extent, with massive to semimassive sulfide bodies. Narrow veins (up to mm width) of secondary serpentine ± calcite ± pyrite (or goethite near the surface) are commonly observed in these samples. The timing of the shear deformation is unclear.

Pentlandite in some near-surface samples is pervasively altered to violarite. Abundant magnesite is found in a sample from the near-surface, and may be related to weathering.

TABLE 2. ORTHOPYROXENE COMPOSITIONS, JINCHUAN ULTRAMAFIC INTRUSIVE COMPLEX, WESTERN CHINA

	Opx in olivine			Opx in matrix		
	Mean	St.Dev.	St.Error	Mean	St.Dev.	St.Error
SiO_2 wt.%	56.84	0.45	0.18	55.71	0.26	0.11
TiO_2	0.02	0.02	0.01	0.63	0.02	0.01
Al_2O_3	0.42	0.32	0.13	1.48	0.10	0.04
Cr_2O_3	0.05	0.05	0.02	0.30	0.11	0.05
FeO	11.29	0.25	0.10	10.09	0.28	0.11
NiO	0.03	0.04	0.02	0.02	0.02	0.01
MnO	0.30	0.10	0.04	0.24	0.04	0.02
ZnO	0.00	0.01	0.00	0.05	0.06	0.02
MgO	30.73	0.33	0.14	29.61	0.30	0.12
CaO	0.07	0.02	0.01	1.51	0.11	0.05
Na_2O	0.02	0.01	0.01	0.06	0.01	0.00
K_2O	0.01	0.01	0.00	0.02	0.03	0.01
Cl	0.01	0.02	0.01	0.01	0.01	0.00
F	0.02	0.02	0.01	0.11	0.10	0.04
Total	99.81			99.86		

St. Dev.: standard error. St. Error: standard error of the mean.

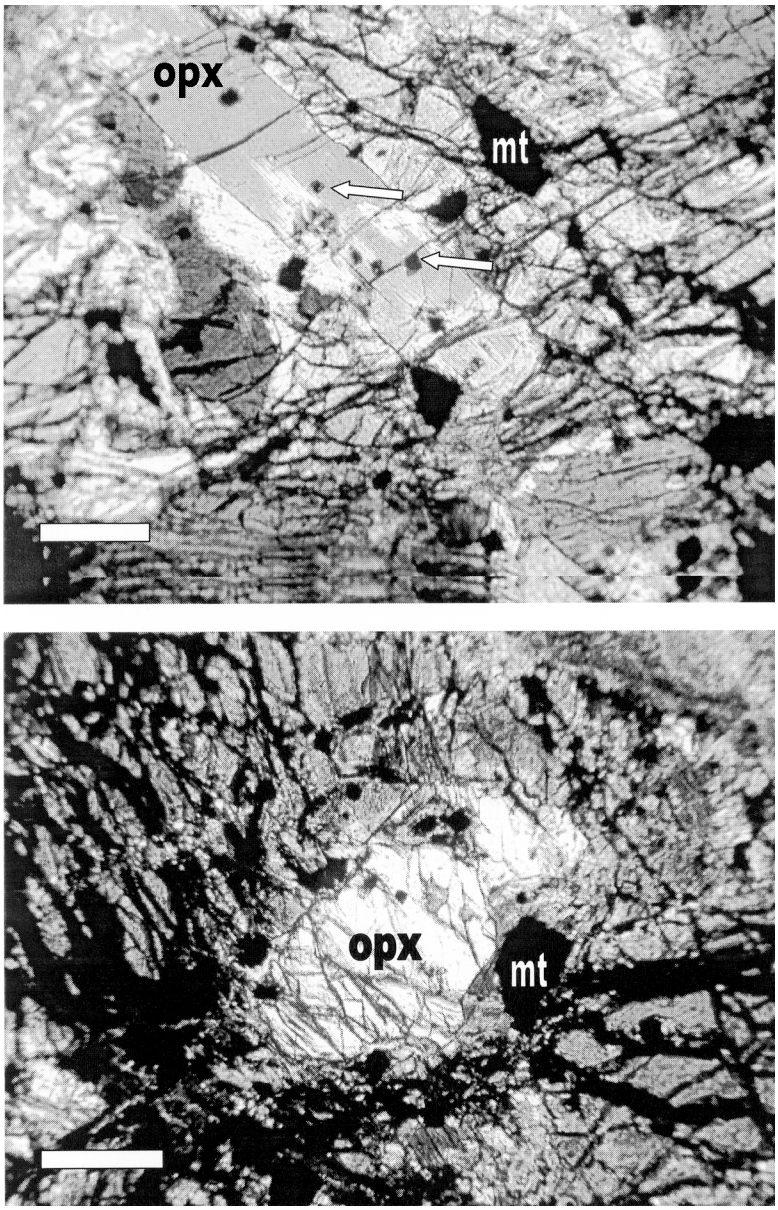

FIG. 5. Early cumulus orthopyroxene crystals (opx) enclosed in cumulus olivine. Arrows mark small crystals of chromian spinel. Olivine is fractured and partly serpentinized. Larger black areas represent secondary magnetite (mt). Scale bars ~ 300 μm.

Whole-rock chemical composition

Representative whole rock compositions of samples containing variable amounts of olivine are listed in Table 3. The data-reduction procedures of the whole-rock chemical data used in this paper are provided in Appendix A.

Nomenclature

Owing to extensive alteration, it is difficult to determine the precise modal quantities of all primary minerals in the rocks by optical observation. Since olivine in the samples exceeds 40 wt%, the rocks may be broadly described as peridotite according to the IUGS nomen-

TABLE 3. SELECTED CHEMICAL DATA, JINCHUAN ULTRAMAFIC INTRUSION

A. Raw data

Sample ID	II14–26	II48–58	I14–21	II14–10	II14–41
Depth m	702	599	165	493	867
SiO_2 wt.%	27.82	28.05	38.54	36.98	44.73
TiO_2	0.11	0.09	0.56	0.33	0.77
Al_2O_3	1.00	1.92	3.86	4.92	7.75
Fe_2O_3	27.70	26.19	13.16	11.42	12.59
MnO	0.17	0.15	0.18	0.17	0.15
MgO	29.33	27.03	30.82	24.42	21.68
CaO	0.21	1.14	3.04	4.08	5.44
Na_2O	0.01	0.01	0.01	0.21	<0.01
K_2O	0.05	0.06	0.33	0.36	0.31
P_2O_5	0.01	0.02	0.08	0.05	0.10
Cr_2O_3	0.67	0.31	0.50	0.43	0.36
NiO	2.65	2.03	0.15	0.14	0.12
V_2O_5	0.01	0.01	0.02	0.02	0.03
ZrO_2	0.00	0.00	0.01	0.00	<0.01
LOI	11.21	11.85	7.75	15.56	5.09
Total	100.95	98.86	98.99	99.07	99.13
As* ppm	3	3	3	3	3
Cu	18172	5483	25	45	318
Ga	2	2	3	10	8
Mo*	1	1	2	2	1
Nb*	2	2	6	2	4
Ni	21760	14534	1209	1069	922
Pb	10	19	12	63	3
Rb*	2	4	14	15	17
Sr	10	31	70	127	47
Th*	3	3	3	5	3
U*	3	3	3	3	3
W*	6	6	6	18	15
Y*	6	5	10	8	12
Zn	113	127	99	152	105
Zr	21	25	64	43	81
Cl	693	512	1092	1699	250
Co	346	285	130	121	113
Cr	3235	1723	3319	3294	2717
Sc	3	4	9	16	16
V	43	46	102	100	149
S (Eltra)	75038	77536	19	994	3627

B. Calculated sulfide fraction as percentage of whole rock

Sample ID	II14–26	II48–58	I14–21	II14–10	II14–41
Depth m	702	599	165	493	867
Chalcopyrite (%)	5.69	1.73	0.01	0.02	0.10
Cobalt pentlandite	0.11	0.09	0.04	0.04	0.03
Pentlandite	6.31	4.83	0.08	0.12	0.08
Pyrrhotite	12.06	18.67	0.00	0.18	0.93
Total sulfide	24.18	25.32	0.13	0.36	1.15

C. Metal content of sulfide fraction

Ni %	8.9	6.5	21.6	11.3	2.4
Co	0.2	0.1	10.6	4.1	1.0
Fe	49.1	57.5	32.4	49.8	60.1
Cu	8.2	2.4	2.0	1.5	2.9
S	33.7	33.5	33.3	33.4	33.5

D. Silicate fraction corrected for LOI and sulfide

SiO_2 wt.%	41.36	43.44	42.13	44.27	47.99
TiO_2	0.17	0.14	0.61	0.40	0.82
Al_2O_3	1.49	2.97	4.22	5.89	8.32
Fe_2O_3 (total)	15.01	8.74	14.32	13.42	12.39
Fe_2O_3	1.50	0.87	1.43	1.34	1.24
FeO	12.16	7.08	11.60	10.87	10.03
MnO	0.25	0.23	0.19	0.20	0.16
MgO	43.60	41.85	33.69	29.24	23.26
CaO	0.31	1.76	3.32	4.88	5.84
Na_2O	0.01	0.01	0.01	0.25	0.00
K_2O	0.07	0.09	0.36	0.43	0.33
P_2O_5	0.01	0.02	0.09	0.05	0.11
Cr_2O_3	1.00	0.48	0.55	0.52	0.39
NiO	0.14	0.13	0.13	0.11	0.09
V_2O_5	0.02	0.02	0.02	0.02	0.03
Total	102.10	99.09	98.36	98.47	98.61
Ni ppm	965	886	1032	873	695
Sr	15	51	76	152	51
Y	10	9	11	10	13
Zr	34	40	70	51	87
Cr	5248	2829	3629	3945	2920
Sc	5	7	10	19	18
V	54	56	111	119	158

* Concentration is close to the limit of detection.

clature (Le Maitre 2002). Alternatively, the CIPW norms may be used for classification. These were calculated using the whole-rock compositions corrected for the presence of sulfides. The amounts of K-feldspar from the CIPW calculation were converted to phlogopite using the equation:

$$\underset{\text{K-feldspar}}{K_2O{\bullet}Al_2O_3{\bullet}6SiO_2} + \underset{\text{olivine}}{[(12x)MgO{\bullet}(6x)SiO_2 + 12(1-x)FeO{\bullet}6(1-x)SiO_2]} + \underset{\text{orthopyroxene}}{[6xMgO{\bullet}6xSiO_2 + 6(1-x)FeO{\bullet}6(1-x)SiO_2]} = \underset{\text{phlogopite}}{K_2O{\bullet}6xMgO{\bullet}6(1-x)FeO{\bullet}Al_2O_3{\bullet}6SiO_2} \quad (1)$$

The distribution of rock types based on the CIPW norms and the IUGS nomenclature (Le Maitre 2002) is illustrated in Figure 6. About 40% of the rocks are olivine-rich norite, gabbronorite and gabbro (color index, M, approaching 90%). The remaining 60% are harzburgite, dunite and lherzolite (M > 90%, ol >> opx + cpx, with small but varying quantities of plagioclase). Only one rock (sample II14–83/2), with approximately 5% olivine, was classified as gabbronorite. This sample, which is intensely sheared and altered, has a composition com-

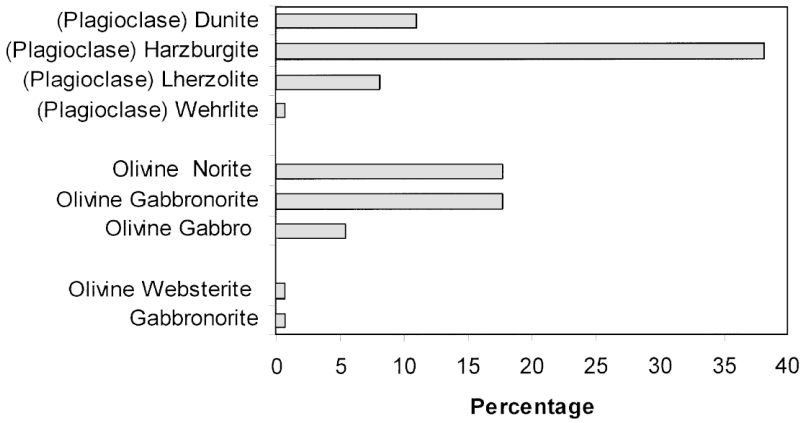

FIG. 6. Relative abundance of rock types in the Jinchuan intrusion derived from normative data (see text for details).

parable to the parental magma for the Jinchuan intrusion proposed by Chai & Naldrett (1992a) (Table 4).

Olivine composition

On the basis of results of 570 electron-microprobe spot analyses, the forsterite content (Fo) of olivine from the samples used in this study varies between 79 and 86 mole %. Figure 7 shows the variation of olivine composition *versus* depth in the three boreholes we have sampled. The profiles are characterized by overall convex-upward curvilinear Fo patterns in olivine with variable local scatter. Borehole II14–83 is characterized by one clear convex pattern, whereas borehole II48–83 is characterized by two juxtaposed convex patterns. The depth profile of Fo contents in olivine for borehole I14–16 is more complicated owing to more pronounced local scatter.

Olivine grain-size distribution

The variation in grain size of olivine may be useful in understanding the emplacement mechanism of the Jinchuan intrusion. The average relative grain-sizes of the ten largest grains per sample (as observed in thin section; see Analytical Methods) are shown in Figure 8. In borehole I14–16, the relative grain-sizes of olivine increase with depth, whereas the opposite is seen in the other two boreholes. The relative grain-sizes for sulfide-poor rocks (borehole I14–16, interval 77–366 m; borehole II48–136, interval 107–310 m) correlate negatively with the amounts of interstitial silicate melt (Fig. 9). The extents of correlation, as indicated by the regression results in both boreholes, are almost identical. Such correlation, however, becomes obscured when the sulfide-rich samples are included. The grain sizes of olivine in the sulfide-rich samples are broadly smaller than in the sulfide-poor samples.

Parental magma

The parental magma of the Jinchuan intrusion may be calculated by assuming that the rocks were formed by variable mixtures of the cumulus phases (olivine, chromian spinel and inclusion-type orthopyroxene) with a homogeneous magma. Limited compositional variation of olivine from samples of variable olivine contents suggests that such an assumption is generally valid for the Jinchuan intrusion. Chai & Naldrett (1992a) were the first to use this method to estimate the composition of the parental magma in the Jinchuan intrusion. Our estimate is statistically not distinguishable from that suggested by Chai & Naldrett (1992a). Accordingly, we used their estimate (Table 4) of the Jinchuan parental magma in all the calculations that follow.

INTERPRETATION AND DISCUSSION

General hypothesis

Any hypothesis addressing the emplacement mechanism of the Jinchuan intrusion will have to explain the following features:

1. The Jinchuan intrusion has a high sulfide-to-silicate ratio. Rough estimates put this ratio at about 0.05. This ratio implies that significant segregation of sulfide took place either before or after emplacement.

2. The profiles through the Jinchuan intrusion drilled to date display a complex lithological structure (Tang 1998a, b). In Figure 10, we reproduce from Tang

& Li (1995) a selection of cross-sections in which lherzolite, plagioclase lherzolite, pyroxene lherzolite, disseminated and net-textured ore display complex layering and discordant relationships. These features are atypical of simple gravity-settling from a ponded magma and more consistent with multiple injections of high-viscosity materials.

3. The occurrence of a "tongue" of relatively dense, net-textured sulfide ore enclosed in a shell of low-density barren rock in the central part of Mining Area II (Fig. 4, Borehole II14–16) is problematic for an *in situ* differentiation model. This tongue-like sulfide body is 600 × 150 × 600 m and open ended at depth. Such a sandwich structure of denser materials in the center requires the intruding materials to be rigid enough to withstand subsequent gravity-collapse after flow eased.

4. The Jinchuan intrusion has a highly variable geometry along strike, ranging from dyke-like in the western section of Mining Area II (borehole II14–16, Fig. 4) to complex lensoid in Mining Areas I and IV (Fig. 10). The dyke-like morphology of the current intrusion may have resulted from differential rotation after emplacement.

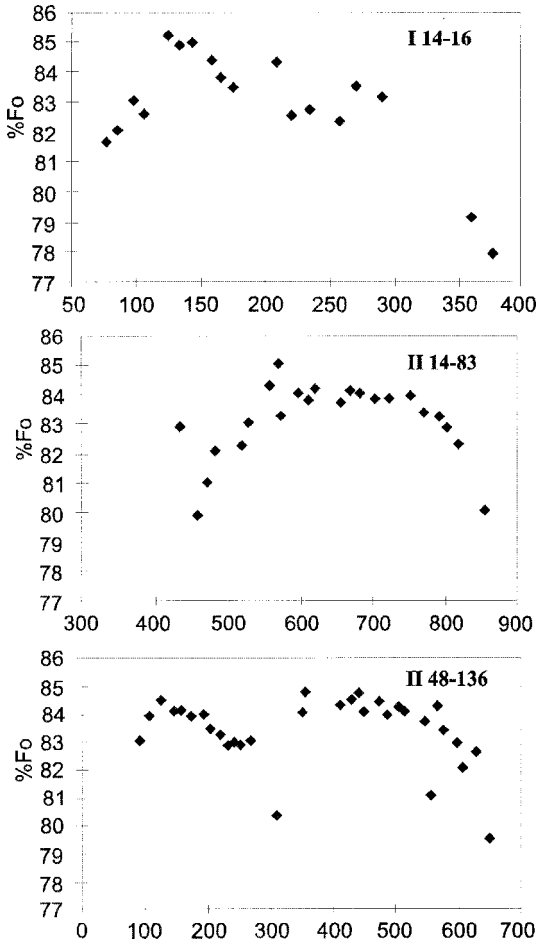

FIG. 7. Variation of Fo content of olivine through boreholes I14–16, II14–83 and II48–136. Curvilinear upward convex patterns are notable. In borehole II48–136, there appear to be two stacked patterns.

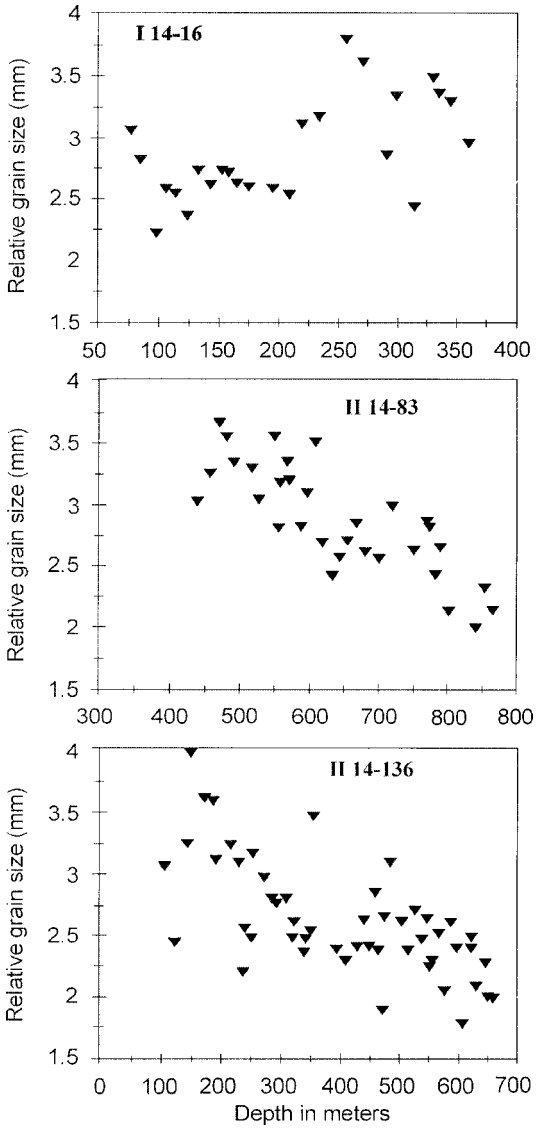

FIG. 8. Variation in relative grain-size with depth (see text for details).

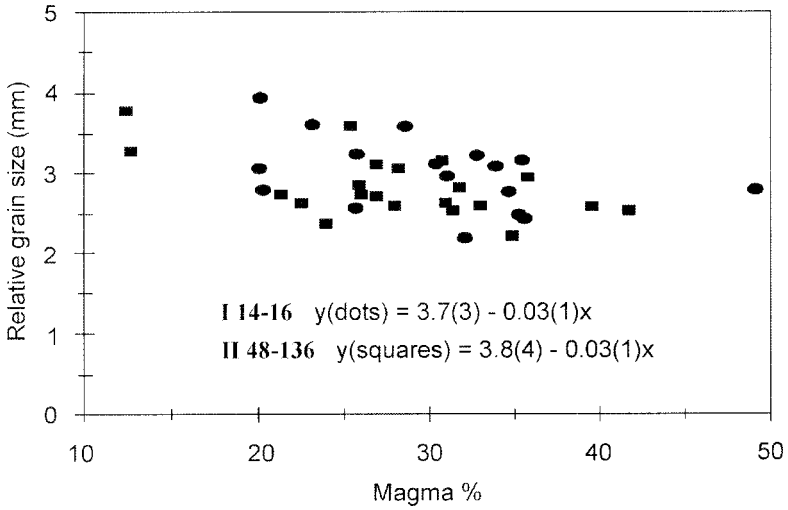

FIG. 9. Relative grain-size correlates negatively with the interstitial liquid content. Data sets from borehole I14–16 (dots) and II48–136 (squares) show almost identical regression equations.

TABLE 4. COMPOSITION OF SAMPLE II14–2 AND OF THE PARENTAL MAGMA AT JINCHUAN

	A	B		A	B
SiO_2 wt.%	51.12	50.8	Ni ppm	491	400
TiO_2	0.51	1.0	Nb	2	8
Al_2O_3	9.75	12.5	Rb	10	30
Fe_2O_3	0	1.0	Sr	338	200
FeO	7.14	11.2	Y	13	20
MnO	0.14	-	Zr	39	100
MgO	13.07	11.5	Sc	38	35
CaO	15.66	10.3	V	210	240
Na_2O	1.17	1.3			
K_2O	0.41	0.8			
Total	98.97	100.4			

A: sample II14–2 (360 m), this study. B: Jinchuan parental magma, Chai & Naldrett (1992b).

In the previous studies, Tang (1998a, b) and Tang & Li (1995) addressed the high sulfide-to-silicate ratio by proposing that sulfide segregated from a mantle-derived ultramafic magma in a deep-seated magma chamber. Gravity settling of sulfide droplets gave rise to liquid stratification, with continuously increasing sulfide content from top to bottom in the chamber. The resulting variable crystal–liquid materials were extracted from the chamber sequentially from top to bottom and emplaced to form a variety of intrusions from sulfide-barren to sulfide-mineralized in the area. They proposed that the sulfide-barren intrusions in the vicinity of Jinchuan were formed by emplacement of the sulfide-poor magmas extracted from the upper parts of the stratified staging chamber, and the Jinchuan intrusion was formed by the sulfide-bearing magma and sulfide liquid extracted sequentially from the lower parts of the staging chamber.

Chai & Naldrett (1992a), on the other hand, argued that the Jinchuan intrusion is the root zone of a large layered intrusion of trumpet shape in cross section, similar to, but smaller than, the Great Dyke of Zimbabwe. Subvolcanic gabbroic cumulates, derived by differentiation from a basaltic magma, originally overlied the ultramafic root-zones but have been eroded away. They argued that in the eastern parts of the intrusion, subhorizontal layering is evidence for settling of cumulus crystals and the concentration of sulfide liquid in response to gravity. They interpreted the dyke-like, central part of the intrusion as a feeder through which magma was fed to the chamber.

In light of our new data, we believe that the overall lithological structure of the Jinchuan intrusion is more consistent with the emplacement of high-viscosity, dense crystal-laden mushes than with that of low-viscosity basaltic magma. The characteristic sill-like geometry with subhorizontal lithological structure in the grid 56 of mining area II (Fig. 10) may represent a better-preserved portion of the originally sill-like body. The steep dip in most parts of the current Jinchuan intrusion is considered to be the result of subsequent rotation of blocks, possibly during regional thrusting. Further, we propose that the mush was originally intruded through pinches and swells of subhorizontal planar fractures and faults. These ideas are further examined below.

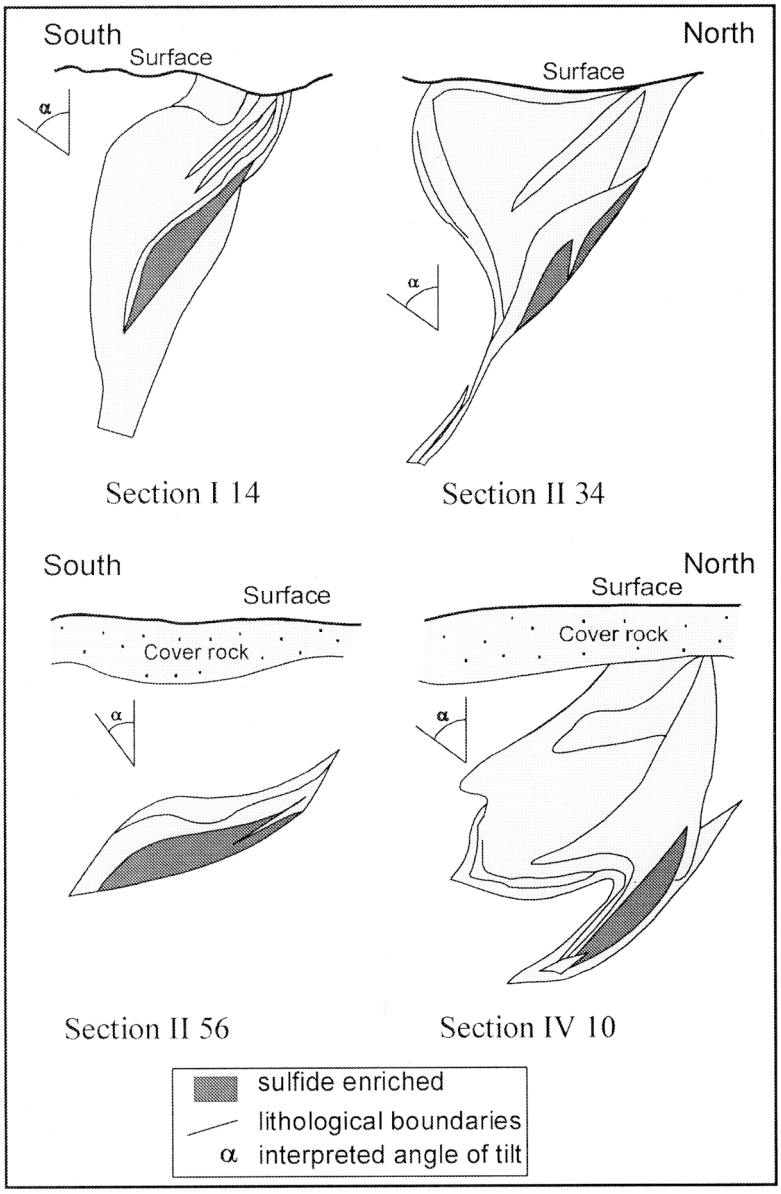

FIG. 10. Selected profiles (adapted after Tang & Li 1995) through the Jinchuan body showing complex lithological boundaries indicative of flow channeling and channel shifting during the intrusion of the mushes. Rapidly varying cross-sectional shapes, as well as the discrete lensoid structure (Section II 56), are noteworthy. Proposed angle of tilt, α, about 30° to 50° to the south. Scales among profiles are roughly similar.

Contents of cumulus phases

Our observations indicate that olivine as well as minor orthopyroxene and chromian spinel are cumulus phases, and silicate and sulfide liquids are intercumulus materials in the Jinchuan rocks. We have calculated the amounts of these constituents in individual samples using the method provided in Appendix B. The depth distribution of the different phases in the boreholes is shown in Figure 11. Borehole II14–83 displays a well-defined, symmetrical pattern of distribution, with sulfide concentrated in the center. The sulfide-rich zone is also characterized by a higher concentration of olivine. Interstitial silicate and sulfide liquids appear to compensate each other. In the olivine-rich zone, as shown in borehole II14–83, the concentration of olivine remains roughly constant throughout at about 75 wt% for the entire interval of ~200 m in thickness. From this "central plateau", cumulus olivine gradually decreases toward the contacts with country rocks. There is some local scatter superimposed on the overall curvilinear patterns of distribution of cumulus olivine.

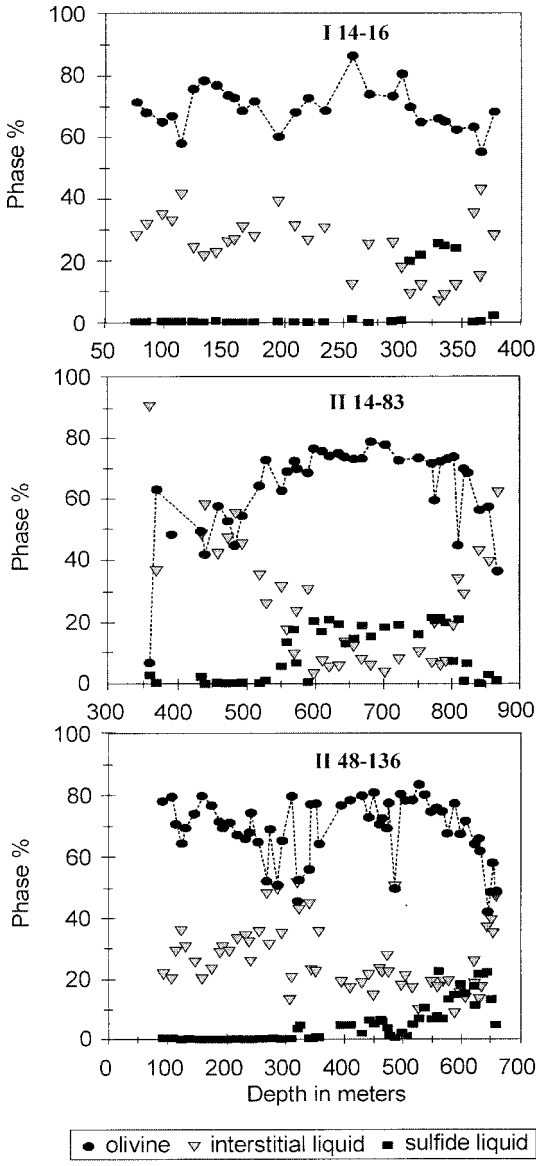

FIG. 11. Variation of cumulus olivine (dots), interstitial silicate magma (triangles) and sulfide (squares) through the three boreholes. Sulfide competes with silicate magma for interstitial space. Broad curved patterns (II14–83 and lower half of II84–136) are interpreted as flow-segregation features, and sharp, high-frequency variations are seen as flow banding (schlieren) structures (see text for details).

The validity of the crystal-mush model for the Jinchuan rocks is supported by the fact that the incompatible trace-element concentrations of Zr, Y V and Sc correlate positively with the estimated amounts of trapped silicate liquid. This relationship, illustrated by Sc in borehole II14–83 (Fig. 12), is to be expected only if the incompatible elements predominantly reside in the interstitial liquid and if our model is correct. Also, the fact that Sc behaves incompatibly supports the observation that pyroxene is not significant as a cumulus phase in the Jinchuan rocks.

In the other two boreholes (I14–16 and II48–136), the sulfide-enriched rocks are concentrated toward the basal contacts (Fig. 11). Symmetrical local variations of cumulus olivine overprint two larger curvilinear distribution patterns in II48–136. In I14–16, the distribution of olivine is dominated by local scatter. Concentrations of incompatible trace elements are well correlated with the amounts of intercumulus silicate liquid in I14–16, but not in II14–83 (Fig. 12).

We propose that the characteristic "central plateau" distribution of olivine in borehole II14–83 (Fig. 12) represents a plug of densely packed mush of olivine + (minor orthopyroxene and chromian spinel) + liquid (silicate and sulfide). As this plug of crystal–liquid material moved along, flow differentiation took placed. Light silicate liquid became more concentrated toward the walls to form a lubricant sheath for the plug. In borehole II48–136, two such plugs, of lesser density than the plug in borehole II14–83, were involved, whereas in borehole I14–16, more than two such plugs may have been involved. Local scatter in the distribution of olivine may have resulted from flow banding and mush mingling in the more chaotic regimes.

Variation of Fo proportions in olivine

A comparison of Figures 7 and 11 shows that olivine from the olivine-rich intervals commonly contains higher Fo than olivine from olivine-poor intervals. In

other words, the Fo content of olivine is negatively correlated with the amounts of interstitial silicate liquid in each borehole (Fig. 13). Such a correlation is consistent with the trapped liquid effect (see Barnes 1986). Metamorphic re-equilibration between olivine and secondary tremolite–actinolite is another process that may have lowered the Fo content of olivine. Because tremolite–actinolite alteration is more prevalent in rocks with a greater proportion of interstitial phases, its effect is complementary to that of the trapped liquid.

Taking into account the effects of trapped liquid crystallization and metamorphism, one sees that the range of Fo contents of the original cumulus olivine is very small, most likely between 85 and 82 mole %. It is difficult to imagine how such a small range of composition of cumulus olivine in the different parts of the intrusion could have been formed by *in situ* fractional crystallization of olivine in a system in which different

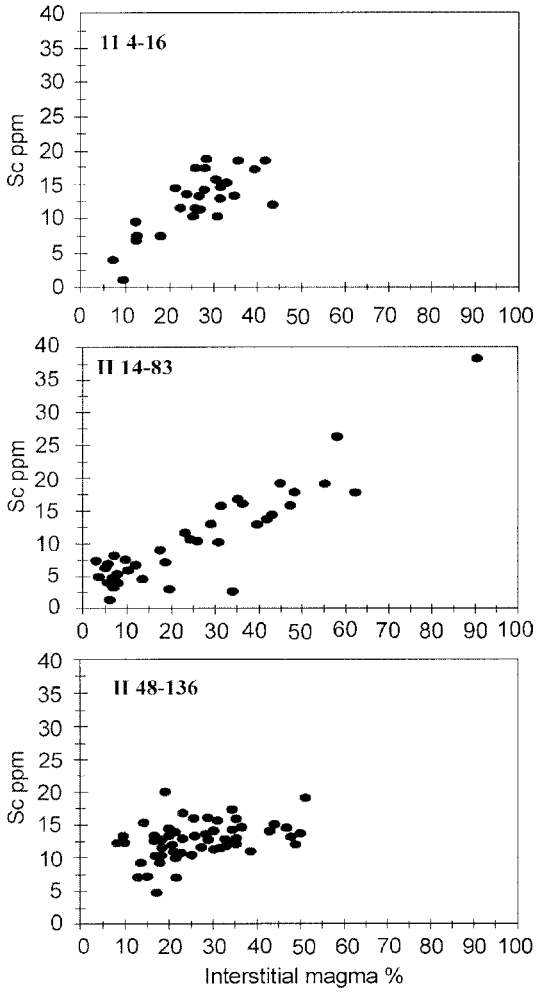

FIG. 12. Linear correlation between Sc and the fraction of interstitial magma is borne out by the data for borehole II14–83 in the center part of the intrusion. The data for the other two boreholes (II48–136 and I14–16) show less linearity, which is interpreted to reflect a more complex mixing history in the latter boreholes.

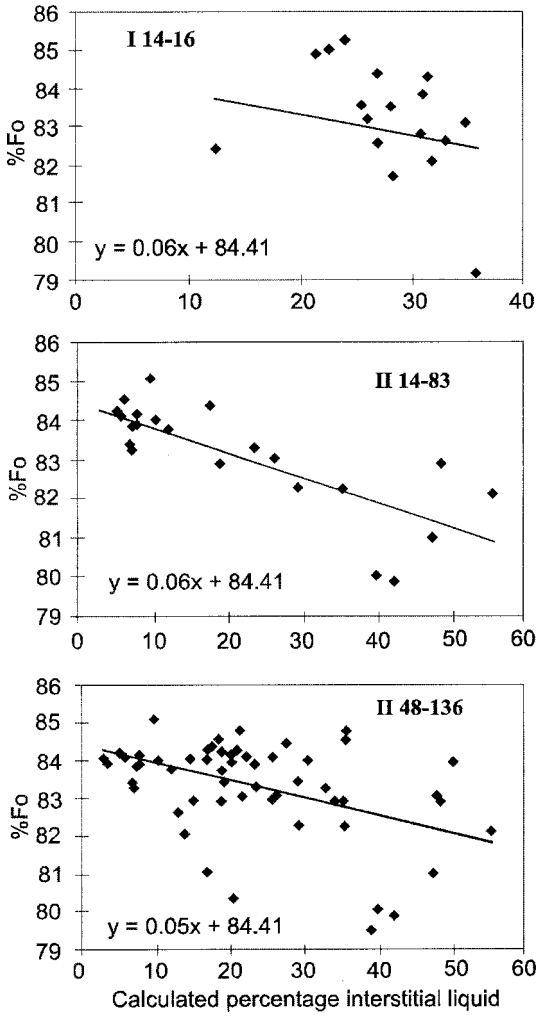

FIG. 13. Fo content plotted against % interstitial silicate liquid. The slopes of the lines are closely comparable, and the trend is interpreted as the combined effect of subliquidus and late metamorphic re-equilibration. For boreholes I14–16 and II48–136, the regression lines were forced through a c intercept at 84.41, a value that was obtained from the regression equation of borehole II14–83.

rates of cooling are to be expected. Preconcentration of cumulus olivine at depth is obviously a better explanation.

Olivine grain-size distribution

The relative grain-sizes of olivine are not correlated with either composition (Fig. 7) or abundance (Fig. 11). The weak negative correlation between olivine grain-size and the amount of interstitial liquid in the rocks (Fig. 9) indicates no significant subliquidus overgrowth of olivine, particularly in the sulfide-rich samples. These features are again inconsistent with *in situ* olivine crystallization. Homogeneous thermal conditions, as expected from a large magma chamber, may have played an important role in producing similar grain-sizes of olivine. Differential rates of cooling in a small body such as the current Jinchuan intrusion would have yielded symmetrical grain-size variations in a cross-section, *i.e.,* small grains along the contacts in view of rapid cooling in this area, and large grains in the central parts owing to slow cooling in this area.

Densities

We have calculated the densities of the proposed mushes from published data on olivine, chromian spinel, orthopyroxene, chalcopyrite, pyrrhotite and pentlandite (Table 5), as well as the calculated densities for the parental magma (Bottinga & Weill 1970) and sulfide liquid (we assumed $\text{density}_{\text{sulfide liquid}} = 0.9 \bullet \text{density}_{\text{solid sulfide}}$). The results are illustrated in Figure 14.

Keeping in mind that the density of the mush is essentially controlled by olivine, interstitial silicate melt and interstitial sulfide liquid, the central borehole (II14–83) displays a symmetrical pattern of density, with the upper (above ~500 m) and lowermost (below 850 m) parts showing densities below 3.1 g/cm^3. Density also mimics the "central plateau" distribution observed for olivine (Fig. 11).

In contrast, the eastern (II48–136) and western (I14–16) boreholes show mutually comparable patterns of density distribution, with the more dense material concentrated toward the base, but not immediately against the footwall. The lowest densities in these boreholes

TABLE 5. COMPOSITION AND DENSITY OF MINERALS USED IN THE CALCULATIONS

	Olivine	Chromian spinel	Orthopyroxene
SiO_2 wt.%	40.03	0.11	56.71
TiO_2	0.00	1.87	0.02
Al_2O_3	0.00	12.08	1.00
Fe_2O_3	0.00	0.00	0.00
FeO	14.20	44.12	12.19
MnO	0.20	0.47	0.31
MgO	45.06	2.52	30.47
CaO	0.11	0.02	0.10
Na_2O	0.00	0.01	0.01
K_2O	0.00	0.00	0.00
P_2O_5	0.00	0.00	0.00
Cr_2O_3	0.01	34.08	0.08
NiO	0.23	0.08	0.03
Total	99.85	95.36	100.92
Density g/cm^3	3.39	5.00	3.32

Density of sulfides: chalcopyrite 4.20, pentlandite 4.60, pyrrhotite 4.60 g/cm^3.

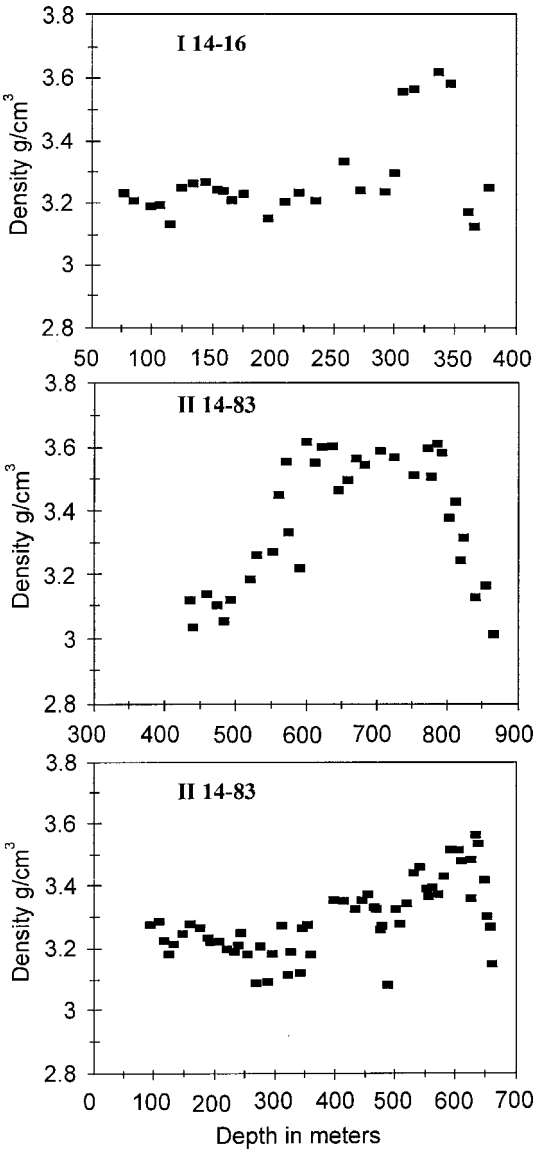

FIG. 14. Calculated densities of the original mushes at liquidus temperatures.

(~3.2 g/cm^3) are, on average, higher than that in II14–83, resulting from the higher concentrations of olivine.

Two important questions arise from the density data. First, under which conditions will such a dense mush move to higher levels in the crust? One may argue that the level of neutral buoyancy for a mush of crystals is on average deeper than the magma chamber in which it forms. A possible answer to the question may be that regional tensional conditions induced the collapse of the roof of the chamber. This idea is in line with the work of Chai & Naldrett (1992a), based on the compositional characteristics of the parental magma for the Jinchuan intrusion; they suggested the presence of a regional tensional environment during the emplacement of the Jinchuan intrusion. Accordingly, we speculate that the injection of magma and crystal mush from a staging magma-chamber to the fault and fracture systems to form the current Jinchuan body was triggered by the collapse of the chamber's roof.

The second question centers on the physical conditions necessary to maintain the original emplacement-related structures, such as the concentric density structure in borehole II14–83 (Fig. 4). In a liquid-dominant system, denser materials will tend to settle and *vice versa*. A crystal mush may be viscous enough to counter such adjustment by gravitational force and thus preserve its original emplacement-related structure. This is further examined below.

Viscosities of the crystal mushes

In the calculations, we used the viscosity approximations of Shaw (1972) for particle-free silicate magmas, and of Gay *et al.* (1969) for crystal-laden silicate magma, as discussed by Pinkerton & Stevenson (1992). According to Gay *et al.* (1969),

$$\eta_0\,(\text{Pa.s}) = \eta_l[\varphi_{max}/(\varphi_{max} - \varphi)]^{2.5} \quad (8)$$

and

$$\eta_{inf}\,(\text{Pa.s}) = \eta_l \exp\{[2.5 + \varphi/(\varphi_{max} - \varphi)^{0.48}]\ \varphi/\varphi_{max}\} \quad (9),$$

where η_0 and η_{inf} are the differential viscosities at low strain-rate and high strain-rates, η_l is the viscosity of the interstitial fluid (magma), φ_{max} is the maximum possible volume concentration of solid particles in a fluid medium, which is a function of size distribution and shape of the solid particles under investigation, and φ is the observed concentration of solids (volume proportions) in the material being investigated. It should be clear that the values of the differential viscosities η_0 and η_{inf} are critically dependent on φ_{max}. As φ approaches φ_{max}, both η_0 and η_{inf} tend toward infinity. The choice of φ_{max} in natural systems is therefore of critical importance.

To estimate the value of φ_{max}, detailed knowledge of the grain-size and grain-shape distributions is needed. Owing to the alteration in the rocks and the inherent topological constraints, we estimated φ_{max} from a plot of the mass ratio of silicate magma / (silicate magma + sulfide liquid) as a function of the volume concentration of olivine crystals. We ignored cumulus orthopyroxene and chromian spinel because their volume proportions and grain-sizes are orders of magnitude smaller than those of olivine. From Figure 15, it is evident that the volume proportion of olivine in the rocks reaches a maximum at about 82%, irrespective of the ratio of silicate magma to silicate magma plus sulfide liquid. This concentration limit most probably marks the point at which the olivine crystals started to jostle against each other to form a solid framework. Accordingly, we used $\varphi_{max} = 82\%$ as being the highest concentration of olivine calculated for the sample set.

Yield strengths were estimated using the formula of Ryerson *et al.* (1988). On the basis of a systematic study, these authors showed that the yield strength of crystal-laden picritic magma, τ_y, is strongly dependent on the crystal content and can be approximated by the formula

$$\tau_y\,(\text{Pa}) = 6500\varphi^{2.85} \quad (10).$$

The calculated viscosities are illustrated in Figure 16. Although only approximations, it is evident that the viscosity of the proposed Jinchuan crystal mushes roughly falls between that of basalt (ln η approximately 2 to 4) and andesite (ln η about 6 to 8). Furthermore, the yield strengths (in Depository for Unpublished Data) increase rapidly with increasing fraction of cumulates, rendering the denser crystal-rich mushes much more resistant to initial mobilization than the less dense ones. The coupled high viscosity and high yield-strength of the crystal mushes may have been critical for the preservation of the concentric and irregular density-structures in the Jinchuan intrusion.

Depth of intrusion

A phase diagram (Fig. 17), constructed with MELTS (Ghiorso & Sack 1995), using the parental magma of Chai & Naldrett (1992a), suggests that

1. Orthopyroxene is the liquidus phase at P = 2.8 kbar (= approximately 9 km depth, at 10 kbar/33 km).

2. Olivine replaces orthopyroxene as the liquidus mineral at 2.8 < P < 1.3 kbar (approximately between 9 and 4 km depth).

3. At P = 1.5 kbar at $f(O_2)$ = QFM, the first olivine to crystallize is Fo_{85}, which compares well with results of the electron-microprobe analyses. Furthermore, only about 5 wt.% olivine crystallizes before orthopyroxene appears on the liquidus. At that point, olivine has reached Fo_{82} in composition.

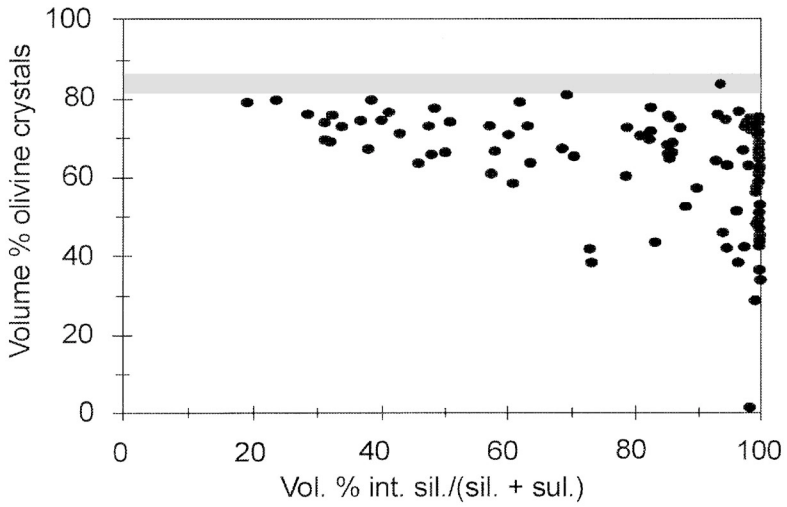

FIG. 15. Variation of volume % cumulus olivine plotted against the percentage of silicate magma in the interstices. The volume fraction of olivine reaches a ceiling at about 82%, which is taken as an indication of φ_{max} (sil. and sul.: fractions of interstitial silicate liquid and sulfide liquid, respectively).

4. Below 1.3 kbar, orthopyroxene does not become stable in the crystallization sequence in that olivine is directly followed by clinopyroxene at about 1220°C.

We use these data to infer that the early cumulus orthopyroxene (as inclusions in the cumulus olivine) and the chromian spinel (in turn enclosed in the cumulus orthopyroxene) crystallized at pressures above 2.8 kbar, *i.e.,* deeper than ~9 km. The bulk of the olivine crystallized between roughly 4 and 9 km, the lower limit based on the fact that orthopyroxene appears to dominate over clinopyroxene among the intercumulus phases in the Jinchuan rocks. Our calculations indicate that crystallization of <5 wt% olivine in the staging chamber is required before final emplacement of the resulting crystal mushes in the chamber to form the Jinchuan intrusion.

TABLE 6. WEIGHTED AVERAGE METAL CONTENT OF SULFIDE FRACTION IN THREE SAMPLES FROM JINCHUAN

	I14-16	II14-83	II48-136
Ni %	7.64	9.16	6.66
Cu	5.68	5.05	3.33
Co	0.14	0.18	0.28
Cu/Ni	0.7	0.6	0.5
Co/Ni	0.3	0.2	0.4

Possible post-emplacement rotation

The cross sections of variable dip at Jinchuan (Figs. 4, 10) show that sulfide zones are not confined to the deepest part, but do seem to hug the lower northern sidewalls (*e.g.,* boreholes I14–16 and II48–136). The similar relationship of the sulfide zones with one particular sidewall is apparently independent of the current dip, which suggests that the currently variable dip of the different parts of the intrusion may not be primary, but rather due to subsequent rotation after emplacement. Using the most gently dipping part of the intrusion, such as the section of grid 56 in Mining Area II (see Fig. 10) as a reference of primary orientation, the other sections are estimated to have been rotated counterclockwise from 30 to 50°. The rotation may have taken placed during the regional Longshoushan uplift event.

Proposed genetic model

In view of our results, we propose that the following sequence of events led to the formation of the Jinchuan intrusion. The very early stage began with the ascent of picritic basic magma into a staging chamber in the crust. Incipient crystallization of chromian spinel and orthopyroxene took place during this ascent at a depth below 9 km. After the magma reached the staging chamber, olivine replaced orthopyroxene on the liquidus, and the crystallization of olivine proceeded. At the same time, sulfide droplets started to exsolve from the magma. Both olivine crystals and sulfide droplets settled down to the bottom of the chamber in response to gravity. The sulfide droplets, being relatively fluid and dense, coa-

lesced, trickled down and partly displaced the interstitial silicate magma of the olivine cumulates at the base of the staging chamber. This displacement of intercumulus silicate melt by sulfide liquid in the bottom layer of the magma chamber increased with depth, and a pure sulfide layer was eventually formed right at the bottom of the chamber. Such a crystal–liquid differentiation process produced a stratified sulfide – olivine – magma column similar to that described in the billiard ball model of Naldrett (1973). Crystal overgrowth ceased once olivine crystals became engulfed in a sulfide liquid, resulting in variable grain-sizes and similar compositions of olivine (Fo value) in the sulfide-rich layer close to the bottom of the chamber. The overlying crystals of olivine forming a framework of jostling crystals neutralized the buoyancy forces. A crystal-mush layer, comprising olivine, orthopyroxene and chromian spinel, was thus formed overlying the sulfide-rich layer.

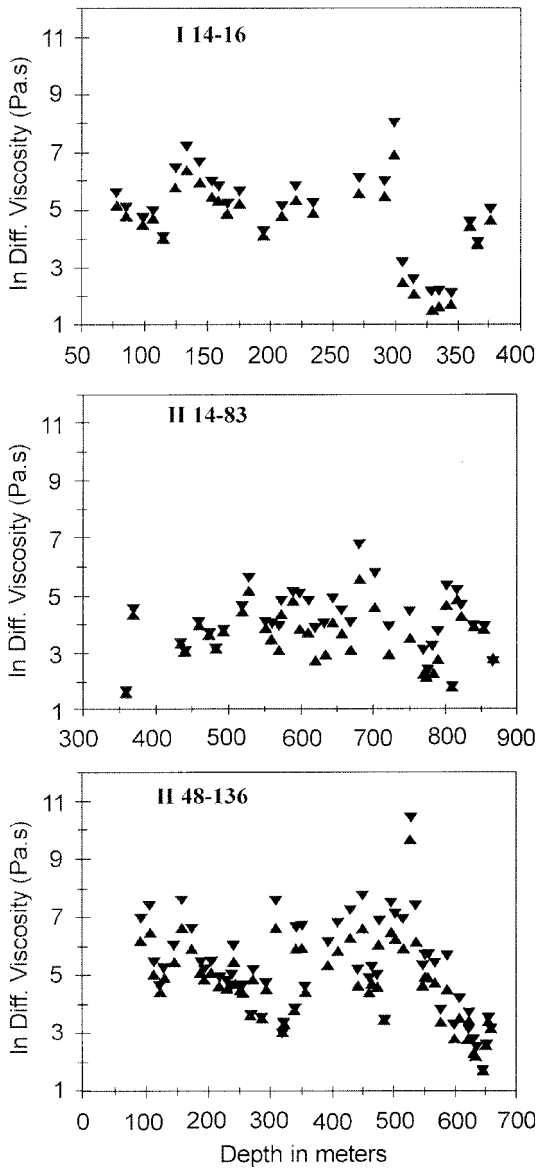

FIG. 16. Calculated differential viscosities, η_0 (inverted triangles) and η_{inf} (triangles) for the Jinchuan crystal/magma mushes at liquidus temperatures (see text for detail).

The second stage was the injection of the bottom-resident sulfide – olivine – magma mushes into planar fractures or faults connected to the chamber. The injection may have been triggered by the collapse of the roof of the chamber under regional tensional conditions. The upper crystal-free magma with relatively low yield-strength and viscosity is the first to be squeezed out of the staging chamber. This led to the formation of some of the sulfide-barren mafic intrusions in the Jinchuan area (Tang 1998a, b).

Following these early tappings of the upper crystal-poor magma, the high yield-strength, relatively viscous, high-density olivine- and sulfide-laden mushes in the bottom of the chamber were injected into nearby planar fractures or faults to form the Jinchuan intrusion. The original depth of the Jinchuan intrusion is estimated to be >4 km, on the basis of phase relationships of cumulus olivine and orthopyroxene in the rocks.

In this model, the central part of the intrusion (borehole II14–83) is interpreted to represent the proximal part of the conduit through which the mushes ascended into the Jinchuan structure. Olivine crystals and sulfide liquid became further concentrated in the center of the conduit in response to a higher velocity in this regime. The western and eastern parts of the intrusion (boreholes I14–16 and II48–136, respectively) are interpreted to represent more distal fronts of the intruding mushes. Fluid dynamics was more chaotic in the distal fronts, resulting in more complex mingling of batches of mush and flow banding in these regimes.

As discussed above, the high viscosity and high yield-strength of the mushes may have played a critical role in preventing the collapse of the original variable-density structures in the various parts of the intrusion after mush emplacement. The original orientation of the Jinchuan structure is more likely a subhorizontal sill-like form rather than the current dyke-like form. The high angle of dip seen today in the intrusion is thought to have resulted from subsequent counterclockwise (looking west) block rotation that took place after mush emplacement and perhaps during the regional Longshoushan period of uplift.

The Jinchuan intrusion was overprinted by low-grade metamorphism and hydrothermal alteration. This may have been associated with the regional uplift. Finally, the exposed and near-surface parts of the intrusion were oxidized and weathered.

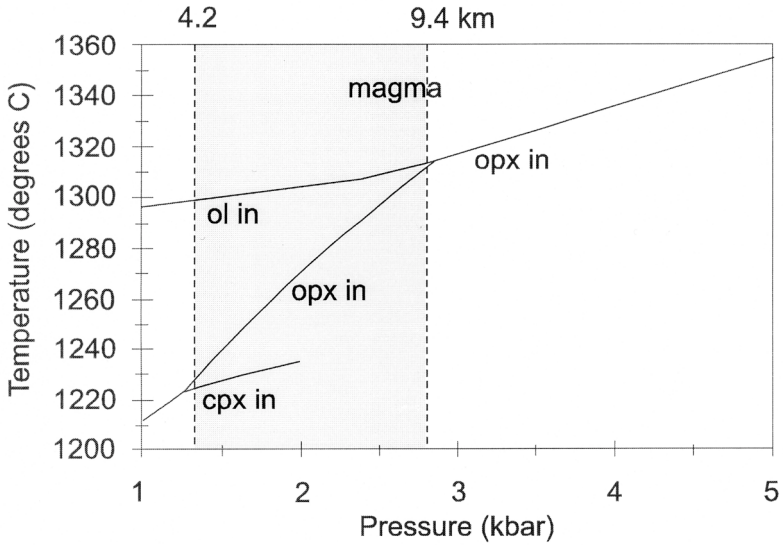

FIG. 17. Calculated phase-diagram, using MELTS, illustrating the probable depth (between ~9 and ~4 km) of the staging chamber of the Jinchuan Intrusion (see text for detail).

CONCLUSIONS

Based on the petrographic observations, variable cross-section geometry and lithological structures, as well as whole-rock compositions, the Jinchuan ultramafic intrusion is interpreted to represent a body of olivine–orthopyroxene–chromian spinel mush. The mush was originally formed in a staging chamber at depth between 4 and 9 km after a small degree of crystallization (<5 wt. % of mostly olivine with minor orthopyroxene and chromian spinel) from a picritic magma. Crystal–liquid density stratification occurred in the staging chamber, resulting in a relatively crystal-free layer at the top and a sulfide-bearing olivine–magma mush at the bottom. The stratified materials were then, sequentially from top to bottom, squeezed out of the staging chamber into fracture and fault systems. The early expulsion of the crystal-poor magma formed the sulfide-barren mafic intrusions in the Jinchuan area and the final expulsion of the olivine- and sulfide-laden mush from the bottom of the staging chamber formed the Jinchuan intrusion. The force of roof collapse possibly induced magma and mush expulsion from the staging chamber. The collapse of the roof in the chamber may have been triggered by regional tension. During mush emplacement at Jinchuan, flow differentiation controlled the proximal, central part of the intrusion, resulting in subconcentric lithological zonation in this regime, whereas chaotic flow prevailed in the distal, eastern and western parts of the intrusion, resulting in complex lithological banding and interfingering. High viscosity and high yield-strength of the mushes prevented the collapse of the original emplacement and flow structures. The high ratio of sulfide to silicate in the Jinchuan intrusion is directly related to sulfide liquid preconcentration in the staging chamber. The original Jinchuan intrusion was probably a sill-like body. It may have been tilted by up to 50° to the south during the regional Longshoushan uplifting.

New in this model are (1) recognition of the importance of the coupled high viscosity and high yield-strength in maintaining the structure of a heterogeneous crystal–liquid system, and (2) identification of early orthopyroxene crystallization that preceded olivine at depth. We agree with Chai & Naldrett (1992a, b) that the parental magma of the Jinchuan intrusion is probably of picritic basalt composition instead of ultramatic composition as proposed by Tang (1998b). We concur with Tang (1998b) that crystal–liquid stratification in a staging magma chamber played an important role in the preconcentration of the sulfide ores in the Jinchuan intrusion.

ACKNOWLEDGEMENTS

The authors express their gratitude to the Research Support Division and the Centre for Research on Magmatic Ore Deposits (CERMOD) of the University of Pretoria for financial support. The research of Chusi Li was partially supported by a grant (EAR 0104580) from the U.S. National Science Foundation. We also thank Rina White for drafting of the figures and Lizelle van

Rooyen for grain-size determinations. A special word of appreciation goes to Bill Meurer, Guest Associate Editor, for his choice of referees and clear guidance on how to improve the manuscript. The valuable comments of Christian Tegner and Alan Boudreau, who refereed the original paper, are acknowledged. We also thank Wolfgang Maier for his critical comments and interest in the paper.

References

BARNES, S.J. (1986): The effect of trapped liquid crystallization on cumulus mineral compositions in layered intrusions. *Contrib. Mineral. Petrol.* **93**, 524-531.

_____ & TANG, Z.L. (1998): Chromites from the Jinchuan, Yejili and Zangbutai intrusions, Gansu Province, China. *In* Mineralization Method of Magmatic Sulfide Deposits (X. Jiang & T. Bai, eds.). Beijing Geological Publishing House, Beijing, People's Republic of China (70).

_____ & _____ (1999): Chrome spinels from the Jinchuan Ni–Cu sulfide deposit, Gansu province, People's Republic of China. *Econ. Geol.* **94**, 343-356.

BENNETT, H. & OLIVER, G. (1992): *XRF Analysis of Ceramics, Minerals and Applied Materials*. John Wiley & Sons, West Sussex, U.K.

BOTTINGA, Y. & WEILL, D.F. (1970): Densities of liquid silicate systems calculated from partial molar volumes of oxide components. *Am. J. Sci.* **269**, 169-182.

CHAI, GANG & NALDRETT, A.J. (1992a): The Jinchuan ultramafic intrusion: cumulate of a high-Mg basaltic magma. *J. Petrol.* **33**, 277-303.

_____ & _____ (1992b): Characteristics of Ni–Cu–PGE mineralization and genesis of the Jinchuan deposit, northwest China. *Econ. Geol.* **87**, 1475-1495.

_____ & _____ (1994): Pyroxene mineral chemistry of the Jinchuan intrusion, China. *Mineral. Petrol.* **51**, 1-20.

_____, _____, RUCKLIDGE, J.C. & KILIUS, L.R. (1993): In situ quantitative analyses for PGE and Au in sulfide minerals of the Jinchuan Ni–Cu deposit by accelerator mass spectrometry. *Can. Mineral.* **31**, 19-30.

GAY, E.C., NELSON, P.A. & ARMSTRONG, W.P. (1969): Flow properties of suspensions with high solid concentrations. *Am. Inst. Chem. Eng. J.* (*AICHEJ*) **39**, 361-383.

GHIORSO, M.S. & SACK, R.O. (1995):Chemical mass transfer in magmatic processes. IV. A revised and internally consistent thermodynamic model for the interpolation and extrapolation of liquid–solid equilibria in magmatic systems at elevated temperatures and pressures. *Contrib. Mineral. Petrol.* **119**, 197-212.

JIA, E.H. (1986): Geological characteristics of the Jinchuan Ni–Cu sulfide deposit in Gansu province *Mineral Deposits* **5**, 27-37 (in Chinese).

LE MAITRE, R.W., ed. (2002): *A Classification of Igneous Rocks and Glossary of Terms*. Blackwell Scientific Publications, Oxford, U.K.

LI, T.L. & CONG, B.L. (1980): A preliminary study on the evolution of the Earth's crust in the North China fault block region. *In* Formation and Development on the North China Fault Block Region (W.Y. Zhang, ed.). Beijing Publishing House of Academy, Beijing, People's Republic of China (in Chinese, 23-35).

NALDRETT, A.J. (1973): Nickel sulfide deposits – their classification and genesis, with special emphasis on the deposits of volcanic association. *Can. Inst. Mining Metall., Bull.* **66**(739), 45-63.

PAN, YANGYANG (1986): Archaean greenstone belt on the Alashan block. *Scientia Geologica Sinica* **3**, 216 (abstr.).

PINKERTON, H. & STEVENSON, R.J. (1992): Methods of determining the rheological properties of magmas at subliquidus temperatures. *J. Volc. Geotherm. Res.* **53**, 47-66.

ROEDER, P.L. & EMSLIE, R.F. (1970): Olivine–liquid equilibrium. *Contrib. Mineral. Petrol.* **29**, 275-289.

RYERSON, F.J., WEED, H.C. & PIWINSKII, A.J. (1988): Rheology of subliquidus magmas. 1. Picritic compositions. *J. Geophys. Res.* **93**, 3421-3436.

S. G. U. (THE SIXTH GEOLOGICAL UNIT OF GANSU PROVINCE, CHINA) (1984): *Geology of the Baijiazuizi Cu–Ni sulfide deposit*. Beijing Geological Publishing House, Beijing, People's Republic of China (in Chinese).

SHAW, H.R. (1972): Viscosities of magmatic liquids: an empirical method of prediction. *Am. J. Sci.* **272**, 870-893.

SHI, Z. (1980): *Mineralogy and Petrology of Ultramafic Rock Body of Jinchuan Deposit*. Bulletin of the Xi'an Institute of Geological and Mineral Resources, Chinese Academy of Geological Sciences (in Chinese).

TANG, Z.L. (1982): Mainly types of Ni deposits of China and their association with the plate tectonics. *Deposit Geology* **2**, 1-14 (in Chinese).

_____ (1990): Mineralization model of the Jinchuan sulfide Cu–Ni deposit. *Modern Geology* **4**, 55-64 (in Chinese).

_____ (1992): Types and geological correlation of the super large magmatic sulfide deposits. *J. Gansu Geology* **1**, 24-47 (in Chinese).

_____ (1998a): Main mineralization mechanism of magmatic sulfide deposits. *In* Mineralization Method of Magmatic Sulfide Deposits (X. Jiang & T. Bai, eds.). Beijing Geological Publishing House, Beijing, People's Republic of China (70).

_____ (1998b): Genetic model of the Jinchuan nickel–copper deposit. *In* Mineralization Method of Magmatic Sulfide Deposits (X. Jiang & T. Bai, eds.). Beijing Geological Publishing House, Beijing, People's Republic of China (70).

_____ & LI, W.Y. (1991): Study and prospect on mineralization pattern of Ni sulfide deposits of China. *Deposit Geology* **3**, 198-203 (in Chinese).

_____ & _____ (1995): *The Genetic Model and Geological Contrast on the Jinchuan Bearing Platinum Ni–Cu Sulfide Deposit*. Beijing Geological. Publishing House, Beijing, People's Republic of China (in Chinese).

_____ & REN, D.J. (1987): The types of Ni sulfide deposits of China. *J. Geol.* **4**, 350-369 (in Chinese).

_____, _____, XUE, Z.R. & WU, Y.K. (1989): *Nickel Deposits of China* **1**. Beijing Geological Publishing House, Beijing, People's Republic of China (205-262).

_____, YANG, J., XU, S., TAO, X. & LI, W. (1992): Sm–Nd dating of the Jinchuan ultramafic rock body, Gansu, China. *Chinese Science Bull.* **37**, 1988-1991.

WATSON, J.S. (1996): Fast, simple method of powder pellet preparation for X-ray fluorescence analysis. *X-Ray Spectrom.* **25**, 173-174.

YANG, ZUN-YI, WANG, HONG-ZHEN & CHEN, YU-GI (1986): *The Geology of China*. Oxford University Press, Oxford, U.K.

ZHANG, Z.M., LIU, J.G. & COLEMAN, R.G. (1986): An outline of the plate tectonics of China. *Geol. Soc. Am. Bull.* **95**, 295-312.

Received November 25, 2002, revised manuscript accepted August 12, 2003.

APPENDIX A. RECALCULATION OF RAW DATA TO ESTIMATE VOLATILE-FREE UNOXIDIZED WHOLE-ROCK COMPOSITIONS

The whole-rock compositions used in this paper are available from the Depository of Unpublished Data of CISTI, National Research Council, Ottawa, Ontario K1A 0S2, Canada. The following arguments and procedures have been used in the recalculation of the raw data to volatile-free unoxidized compositions.

The raw data showed variable but large LOI components, which attested to the strongly hydrated state of the rocks. Furthermore, the totals of the major elements (determined on fused bead) were low where the S content was high. This was interpreted to be largely due to the fact that with high S, Cu becomes a major element, but is not determined on the fused glass bead.

To arrive at more meaningful estimates of the compositions of the volatile-free unoxidized (by roasting) compositions, and assuming that during the roasting step, 1) all H_2O and CO_2 are driven off, 2) all S is vaporized (complete depletion in the residual powder), 3) Cu, Ni, Co and Fe, all in sulfide, are oxidized to CuO, NiO, CoO and Fe_2O_3, respectively, and 4) FeO in the silicate phases is oxidized to Fe_2O_3, we made following corrections. Starting from

$$\sum_{i=1}^{n} c(i) + \text{LOI} = \text{Total A} \quad (1)$$

where c(i) is the concentration of the i^{th} oxide in the fused bead, Cu was added to give the new total

$$\sum_{i=1}^{n} c(i) + \text{LOI} + \text{Cu} = \text{Total B} \quad (2).$$

As the rocks contain variable amounts of (Cu,Ni,Fe,Co) sulfide, as well as hydrous phases and carbonates,

$$\text{LOI} = H_2O + CO_2 + S - O(Cu) - O(Ni) - O(Co) - O(Fe) - O\,(Fe^{2+}/Fe^{3+}) \quad (3)$$

where O(Cu), O(Ni) refer to the mass of oxygen that replaces S during the roasting process, and O (Fe^{2+}/Fe^{3+}) is the oxygen needed to oxidize the ferrous iron in silicate to ferric iron. If O replaces the entire S, then it follows that

$$O(Cu) + O(Ni) + O(Co) + O(Fe) = 0.5\ S + O(FeO/O_{1.5}) \quad (4)$$

where $O(FeO/O_{1.5})$ is the oxygen needed to take the FeO derived from FeS to Fe_2O_3. Combining equations 2, 3 and 4, and re-arranging, we get

$$H_2O + CO_2 = \text{Total B} - \sum_{i=1}^{n} c(i) - \text{Cu} - 0.5\ S - O(FeO/O_{1.5}) + O\,(Fe^{2+}/Fe^{3+}) \quad (5)$$

where $O(Fe^{2+}/Fe^{3+}) = 0.136FeO$ (in silicate). The Fe in the silicate fraction can be approximated by

$$\text{Fe(sil)} = \text{Fe(total)} - \text{Fe(sul)} = \text{Fe(total)} - 0.573[S - 0.504Cu - 0.545Ni] \quad (6).$$

FeO in silicate can be estimated by assuming some fixed ratio of ferrous to ferric iron in the silicate fraction. Following this approach, corrections for H_2O and CO_2, as well as for the various oxidation-induced processes during roasting, can be made to arrive at corrected estimates of the volatile-free whole-rock compositions.

For the calculation of the sulfide fractions in the rocks, we assumed the mineral compositions for pyrrhotite, pentlandite, cobalt pentlandite, and chalcopyrite to be Fe_7S_8, $Ni_{4.5}Fe_{4.5}S_8$, $Co_{4.5}Fe_{4.5}S_8$ and $CuFeS_2$, respectively. Ni in silicate was determined from the relation: log Ni (ppm) = 0.016 MgO (%) + 2.475, which was obtained from a plot of log Ni against MgO of a selection of sulfide-poor rocks (after LOI and oxidation correction). The fraction of sulfide in each rock was then calculated from S in the order pentlandite, cobalt pentlandite, chalcopyrite and pyrrhotite, until all sulfur was consumed. In the tables of deposited data, we list the calculated composition of the sulfide fraction and the metal contents of the sulfide fraction (*i.e.*, metal in 100% sulfide). The average metal contents of the sulfide fractions in the three boreholes are summarized in Table 6. Although there is a significant variation in the total metal values from one borehole to the next, the metal ratios are practically constant. These data suggest a slight variation in R factor (ratio of total silicate to exsolved sulfide melt), but a constant composition for the equilibrating silicate magma.

The calculated compositions of the sulfide-free silicate fraction in the rocks are also listed in the tables of deposited data. Of all the final totals, only about 6% fall outside the accepted range of 98 to 102%. This discrepancy is probably the result of various factors ranging from uncertainties about the final state of the roasted products to minor analytical error. Of particular importance is the fact that one assumes a constant degree of postmagmatic oxidation for all samples, an assumption that is most probably invalid, and that adds to the general geological variance. Four samples (I14–11, II14–36, II48–61 and II48–65) gave unrealistic values for the calculated composition of the silicate fraction. We ascribe these discrepancies to the presence of pyrite veins in the relevant rocks (see Appendix B).

APPENDIX B. CALCULATION OF WEIGHT FRACTIONS OF PHASES IN JINCHUAN MUSHES

As indicated in the petrographic descriptions, the Jinchuan rocks, at the time of emplacement, probably comprised crystal mushes with olivine, chromian spinel and orthopyroxene set in a matrix of silicate magma and sulfide liquid. It follows that

$$\mathrm{cs(i,j)} = a.\mathrm{co(i,j)} + b.\mathrm{cp(i,j)} + d.\mathrm{cc(i,j)} + e.\mathrm{cm(i,j)} + f.\mathrm{fe(j)} \quad (7)$$

where a, b, d and e are fractions and cs(i,j), co(i,j), cp(i,j), d.cc(i,j) and cm(i,j) are the i^{th} element oxide in the silicate liquid fraction, olivine, orthopyroxene, chromian spinel, and interstitial magma, respectively, in the j^{th} sample. Since $b = 0.05a$ (assumption) and deriving d from the XRF-established Cr in each rock, the degrees of freedom in equation 7 reduces from 4 to 2. Using the concentrations of SiO_2, TiO_2, Al_2O_3, FeO(total), MgO, CaO, Na_2O, K_2O, Cr_2O_3 and NiO present in all the phases, equation 7 can be solved by least-squares optimization for all j samples. The fractions of olivine, chromian spinel, orthopyroxene, silicate magma and sulfide liquid in the original mushes can thus be estimated.

We noted, during earlier simulations, that FeO(total) was a major source of variance. This is in part due to the way in which the sulfide fraction is calculated. A small error in S will be enhanced in the total iron allocated to pyrrhotite, and hence the FeO reserved for the silicate fraction. A random error in S will cause both over- and underestimation of the FeO in the silicate fraction. However, the variable quantities of pyrite-bearing veins (see section on petrography) present in the Jinchuan rocks, which are not considered in the mass-balance model, are expected to cause significant underestimation of the FeO in the silicate fraction. On the other hand, the goethite veins (see section on petrography) will lead to overestimation of FeO. To counteract this source of error, we introduced the term, f.fe (f = fraction, fe = 100% FeO) in equation 7 as a slack variable to absorb variations in iron content due to Fe-rich phases not accounted for in the model. The coefficient f assumed a value of -0.6 ± 2.68% for the 124 samples treated. The negative tendency of this factor indicates that the iron content of the silicate fraction, in general, was underestimated, which could be due to the presence of pyrite veins in the rocks. This underestimation was particularly large for samples I14–11, II14–36, II48–61 and II48–65.

In the final model, the average deviation per element oxide (*i.e.*, measured minus calculated) over the 124 samples calculated to 0.6, 0.05, 0.3, 0.1, 0.1, 0.3, 0.1, 0.06, 0.07 and 0.01 absolute % for SiO_2, TiO_2, Al_2O_3, FeO(total), MgO, CaO, Na_2O, K_2O, Cr_2O_3 and NiO, respectively. The low values support the validity of the model used here.